American Journal of Engineering and Applied Sciences

Original Research Paper

Large Scale Synthesis of ZnO Nanostructures of Different Morphologies through Solvent-free Mechanochemical Synthesis and their Application in Photocatalytic Dye Degradation

[1]Raúl Sánchez Zeferino, [2]Jesús Alberto Ramos Ramón, [2]Ma. Eunice de Anda Reyes, [2]Rutilo Silva González and [2]Umapada Pal

[1]Departamento de Física, Universidad de Sonora, Apdo. Postal 1626, Col. Centro, Hermosillo 83000, Sonora, Mexico
[2]Instituto de Física, Benemérita Universidad Autónoma de Puebla, Apdo. Postal J-48, Puebla, Pue. 72570, Mexico

Article history
Received: 28-10-2015
Revised: 08-12-2015
Accepted: 13-01-2016

Corresponding Author:
Umapada Pal
Instituto de Física, Benemérita Universidad Autónoma de Puebla, Apdo. Postal J-48, Puebla, Pue. 72570, Mexico
Email: upal@ifuap.buap.mx

Abstract: Well crystalline, near-stoichiometric zinc oxide nanostructures of different morphologies are fabricated in large scale, utilizing a simple, cost effective mechanochemical synthesis in absence of solvent. Effects of ionic and nonionic surfactants along with the concentration of hydrolyzing agent on the evolution of nanostructure morphology have been studied. It has been observed that while a cationic surfactant such as Cetyltrimethylammonium Bromide (CTAB) favors the nanostructures to growth along their polar c-axis, a nonionic surfactant such as Polyvinylpyrrolidone (PVP) reduces their preferred c-axis growth. Increase of hydrolyzing agent in the reaction mixture enhances the growth rate of the nanostructures. The nanostructures have been tested for photodegradation of anionic dye molecules such as Methylene Blue (MB). All the nanostructures manifest high photocatalytic performance. Apart from morphology, the specific surface area, crystal plane orientation and the concentration of basic sites at surface are seen to contribute significantly to the photocatalytic performance of the zinc oxide nanostructures.

Keywords: ZnO, Nanostructures, Mechanochemical Synthesis, Photocatalysis, Dye Degradation

Introduction

Recent thrust of metal oxide nanostructure research is driven by their application potentials in diverse fields such as gas sensing (Hsu *et al.*, 2008; Kumar *et al.*, 2015; Wang *et al.*, 2006; 2012; Xu *et al.*, 2000), optoelectronic device fabrication (Hsu *et al.*, 2008; Olson *et al.*, 2007; Valerini *et al.*, 2008; Zimmler *et al.*, 2008), catalysis (Matsamura and Ishibe, 2009; Lorenz *et al.*, 2013; Spencer 1999) photocatalysis (Jia *et al.*, 2015; Morales Flores *et al.*, 2014; Ruiz Peralta *et al.*, 2012; Yang *et al.*, 2015) and dye adsorption (Chen *et al.*, 2015; Khosla *et al.*, 2015; Norman, 1970). Due to high thermal and chemical stability and reasonable biocompatibility, the application of metal oxide nanostructures extended further to biology and medicine (Hahn *et al.*, 2012; Hilger and Kaiser, 2012; Solanki *et al.*, 2011). While for each of these applications metal oxide nanostructures of specific nature and characteristics such as size, composition, nature of dopant and morphology are frequently preferred, apart from some basic characteristics such as band gap energy, excitonic energy, photoresponse and specific surface area, the role of other characteristics has not been associated to their performances with certainty. To elucidate the facts, we can consider a specific material, such as zinc oxide, which is a metal oxide semiconductor of high band gap energy (3.37 eV at room temperature) and high excitonic energy (60 meV). In nanostructure forms, it is very much suitable for fabricating optoelectronic and piezoelectric devices (Jalali *et al.*, 2013; Solanki *et al.*, 2011; Wang and Song, 2006), photocatalytic degradation of organic materials (Morales Flores *et al.*, 2014; Ruiz Peralta *et al.*, 2012) and catalytic supports

(Lorenz *et al.*, 2013; Matsamura and Ishibe, 2009; Spencer, 1999). ZnO nanostructures of different morphologies and sizes have been fabricated using a vast number of chemical and physical methods and the roles of their morphology, defect structure and surface area have been studied extensively, especially in the context of later applications (Jalali *et al.*, 2013; Pan *et al.*, 2014; Ruiz Peralta *et al.*, 2012; Wang and Song, 2006). While through physical evaporation process, 1D ZnO nanostructures such as nanorods, nanowires and nanobelts have been fabricated (An *et al.*, 2013; He *et al.*, 2006; Wang *et al.*, 2005; 2004a; 2004b), through chemical processes such as sol-gel (Tak and Yong, 2005), hydrothermal and other solution based synthesis (Chen *et al.*, 2000; Ni *et al.*, 2005; Shao *et al.*, 2008; Xie *et al.*, 2011), ZnO nanostructures of a large variety of morphologies have been fabricated successfully. Utilizing amine-assisted nonhydrolyzing synthesis method, Zhang *et al.* (2007) could fabricate ZnO nanostructures of different morphologies using zinc acetate precursor. On the other hand, utilizing the simple and cheap mechanochemical technique, ZnO nanostructures of different morphologies (Anand *et al.*, 2014; Tsuzuki and McCormick, 2001; 2004; Shen *et al*., 2003) could be synthesized with good control over their shape and size. In fact, a vast number of reports have been published on the morphology control of ZnO nanostructures through hard and soft chemical routs and their photocatalytic performances for organic dye degradation under UV illumination. While controlled fabrication of ZnO nanostructures of different morphologies and specific surface areas through cheap and soft chemical routs remains a challenge, understanding the roles of morphology, surface area, defect content and surface acid/base sites on their catalytic and photocatalytic performance is the other task, essential for fabricating suitable ZnO nanostructures for efficient environmental applications.

In the present article, we demonstrate the fabrication of ZnO nanostructures of different morphologies in large scale through a solvent-free soft mechanochemical process, utilizing ionic and non-ionic surfactants (structure driving agents) and NaOH as precipitating/hydrolyzing agent. Effects of morphology, surface area and surface acid/base sites on their photocatalytic dye degradation performance have been studied applying Methylene Blue (MB) as a test dye. It has been demonstrated that the surfactant and concentration of hydrolyzing agent both play important roles for defining the final morphology of ZnO nanostructures. The roles of surfactant and hydrolyzing agent on the evolution of morphology and photocatalytic performance of mechanochemically grown ZnO nanostructures have been discussed.

Experimental

Reagents and Solvents

Analytical grade zinc acetate dihydrate [$Zn(CH_3COO)_2•2H_2O$], sodium hydroxide (NaOH), Cetyltrimethylammonium Bromide (CTAB) and polyvinylpyrrolidone (PVP, MW 40,000) were purchased from Sigma-Aldrich, Mexico and used as received without further purification.

Preparation of ZnO Nanostructures using CTAB and PVP

ZnO nanostructures were synthetized through mechanochemical process following the procedure reported by Anand *et al.* (2014) with some modifications. Briefly, Zinc Acetate dihydrate (ZnAc) and CTAB or PVP in 2:1 molar ratio were mixed in a ceramic mortar for about 30 min. After that, a certain amount NaOH was added to the above mixture and manually grinded for another 30 min at room temperature. The molar ratio of ZnAc and NaOH in the mixture was maintained either 1:3 or 1:9. The obtained white pastes were dispersed in water and washed with ethanol and water several times by centrifugation (8000 rpm, 10 min). Obtained samples were dried at room temperature and annealed thereafter at 350°C for 2 h in air. Utilizing 40 mmol of zinc acetate precursor, about 3.0-3.2 g of ZnO nanostructures were obtained for each of the samples. The synthesis conditions used for fabricating different ZnO nanostructures and their nomenclatures are given in Table 1.

Table 1. Preparation conditions, morphology, composition and BET and XRD estimated texture parameters for the fabricated ZnO nanostructures

Sample name	ZnAc/NaOH (molar ratio)	Surfactant used	Morphology	EDS estimated Zn:O (at. ratio)	BET surface area (m^2/g)	BET Av. pore diameter (nm)	XRD estimated Av. crystallite size (nm)
ZnO-1	1:3	———	elongated particles	1.05	16.35	63.1	32.7
ZnO-2	1:3	CTAB (5.4 mmol)	nanorods	1.03	8.72	30.1	38.4
ZnO-3	1:9	CTAB (5.4 mmol)	Flower consisting nanorods (echinoids)	1.02	8.35	46.8	35.2
ZnO-4	1:3	PVP (0.05 mmol)	spherical particles	1.04	12.36	80.5	36.2
ZnO-5	1:9	PVP (0.05 mmol)	flowers consisting petals	1.03	6.90	40.4	33.8

The samples were prepared at Zinc Acetate (ZnAc) and NaOH molar ratios of 1:3 and 1:9 for a fixed molar content of surfactants CTAB and PVP to study the effects of surfactant and NaOH concentration on the morphology and photocatalytic behaviors of the fabricated nanostructures. As the growth rate of ZnO nanostructures and their morphology are known to be driven by the surface energy of their crystal facets or planes, which generally get modified by surfactants apart from the pH of the reaction (Xie *et al.*, 2009; Jang *et al.*, 2009), we used CTAB and PVP as ionic (cationic) and non-ionic surfactants, respectively, to observe the effect of surfactant nature on morphology evolution of ZnO nanostructures.

Characterization of the ZnO Nanostructures

The crystallinity and structural phase of the nanostructures were analyzed through powder X-Ray Diffraction (XRD, Bruker D8 Discover) and micro Raman spectroscopy (Horiba Yovin Lab RAM HR). While the XRD patterns of the samples were recorded in 10-70° range utilizing CuKα (λ = 1.5406 Å) radiation in 0.02° 2θ steps, their room temperature Raman spectra were recorded using the 633.8 nm line (10 mW, 1.0 mm spot size) of a He-Ne laser as excitation source and a thermoelectrically cooled charge-coupled device as detector. For morphology and elemental analysis, a JEOL JSM-7800F Field-Emission Scanning Electron Microscope (FESEM) with Oxford X-Max analytical accessory was used. A JEOL JEM 2100F field emission transmission electron microscope (FE-TEM) operating at 200 kV was utilized to study the crystal structure and growth induced defects in the nanostructures. To estimate the specific surface area and average pore size in the nanostructures, their adsorption-desorption isotherms at 77 K were recorded in a Belsorp-Mini II (BEL Japan, Inc.) analyzer. The samples were degassed at 250°C for 5 h under vacuum prior to their analysis. The specific surface area and average pore diameter in the samples were estimated utilizing Brunauer-Emmett-Teller (BET) procedure (Brunauer *et al.*, 1938).

Photocatalytic Evaluation of the ZnO Nanostructures

The photocatalytic responses of the nanostructures were recorded in a Shimadzu UV-3101 PC UV-Vis-NIR double-beam spectrophotometer. The tests were performed in aqueous solution using methylene blue (MB, $C_{16}H_{18}ClN_3S•3H_2O$, Sigma-Aldrich) as a test contaminant. A cylindrical jacketed glass mini-reactor of 500 mL capacity with 50 mm internal diameter and about 120 mm of height was utilized to perform batch reactions. Room temperature MB photodegradation rate of the catalysts was monitored by dispersing 20 mg of powder ZnO sample in 40 mL of MB solution (10 ppm). The catalyst-containing reaction mixture under magnetic agitation was illuminated by a 10 W ultraviolet LED lamp (model JX-10UV9X1B365) of 365 nm emission. The lamp was placed at the top of the reactor, about 13 cm above the test solution surface. The temperature of the reaction mixture was maintained fixed at 25°C by circulating cold water through the jacket of the reactor. Oxygen was bubbled through the reaction solution under UV illumination.

The MB concentration in the reaction mixture was monitored by a computer-controlled spectrophotometer at regular intervals, withdrawing each time about 3.5 mL of the solution (aliquot) from the reactor. To separate the dispersed catalyst from the aliquot, a reusable syringe filter holders (z268410) with nitrocellulose membrane filter of 0.22 mm pore size was utilized. From the absorbance spectra of MB recorded at different time intervals, the concentrations of MB in the reaction solution were estimated using a pre-calibrated concentration curve. The MB concentration in the reaction mixture was determined from the intensity of the most prominent absorption band of MB around 664.5 nm.

Results and Discussion

Figure 1 presents the X-ray diffraction patterns of the samples prepared at different ZnAc:NaOH ratios in absence and presence of surfactants (Table 1). As can be seen, all the samples revealed well resolved, high intensity diffraction peaks correspond to crystalline ZnO in hexagonal wurtzite phase (JCPDS card no. 79-0207). The relative intensity of the main diffraction peaks like (100), (002) and (101) varied a little from sample to sample. No significant shift in the position of the diffraction peaks was observed for the samples prepared at different precursor-NaOH molar ratios or for different surfactants. Utilizing the most intense (101) diffraction peak, average grain size (P) in the ZnO nanostructures was estimated using the Debye Scherrer equation (Cullity and Stock, 1956):

$$P = \frac{K\lambda}{\beta \cos\theta} \tag{1}$$

where, K is the shape factor considered to be 0.9, λ is the X-ray excitation wavelength (λ = 1.5406 Å), β is the FWHM of the (101) peak and θ is the Bragg angle. Estimated average grain size values for the ZnO nanostructures are presented in Table 1. In general, the presence of surfactant (of either nature) enhances the average grain size of the nanostructures. However, apparently the nature of surfactant does not affect their crystallite size. A decrease of average grain size for the nanostructures prepared with higher NaOH content (higher pH of the reaction) is probably due to higher growth rate of the nanostructures at higher reaction pH.

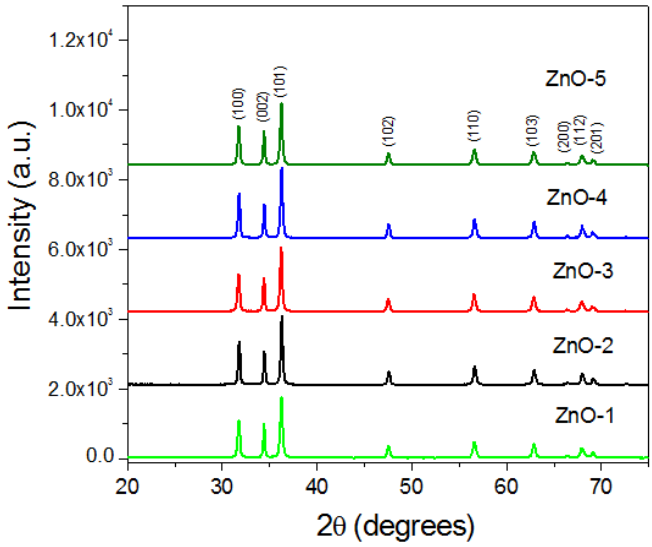

Fig. 1. XRD patterns of the mechanochemically fabricated ZnO nanostructures utilizing CTAB or PVP as surfactant

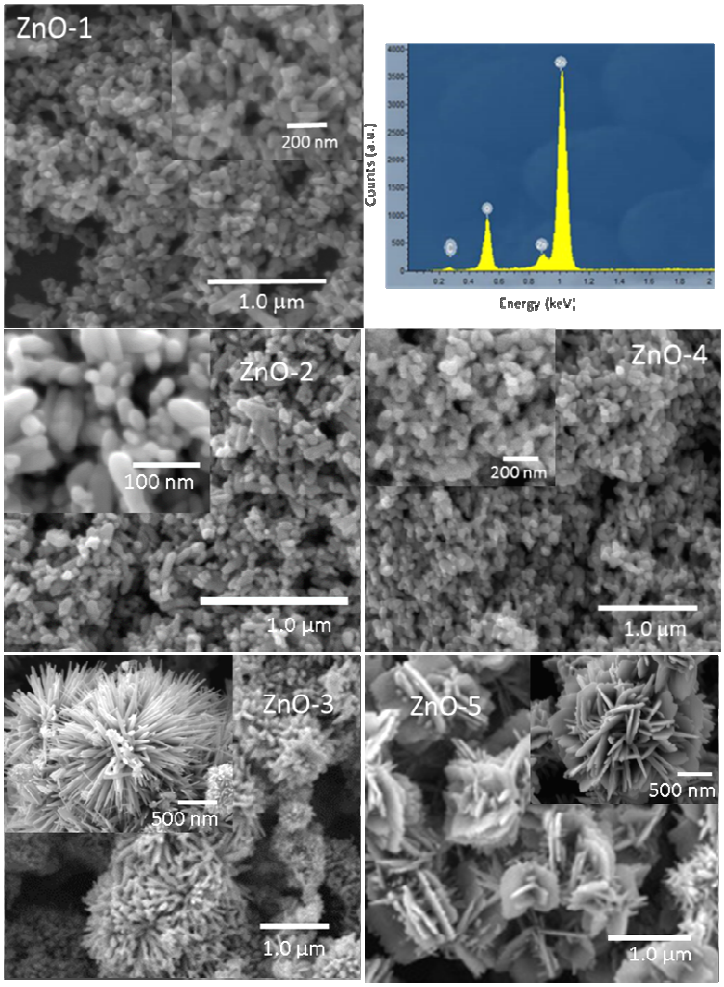

Fig. 2. Typical SEM images of the ZnO nanostructures fabricated by mechanochemical synthesis, along with their typical EDS spectrum

As can be seen from Fig. 2, both the nature of surfactant and hydrolyzer concentration have strong effect on the final morphology of ZnO nanostructures. While in absence of any surfactant, a molar ratio 1:3 of ZnAc and NaOH produces elongated nanoparticles (Fig. 2, sample ZnO-1) of about 77 nm average (*c.a.)* size, presence of CTAB (cationic surfactant) enhances the growth of ZnO along polar c-axis, resulting rod-like 1D nanostructures of about 300 nm average (*c.a.*) length and 50 nm average diameter (*c.a.*). On the other hand, the effect of reaction pH on morphology evolution of ZnO nanostructures is very prominent for both the surfactants. As can be seen from the SEM images of the samples ZnO-3 and ZnO-5 prepared at 1:9 precursor-hydrolyzer molar ratio using CTAB and PVP as surfactant, respectively, the pH of the reaction affects the morphology of ZnO nanostructures severely. While the former sample revealed echinoid like (flower consisting nanorods emanating from a common point) morphology, the later sample revealed rose-like (flower consisting petals) morphology.

The evolution of very distinct morphologies in these two samples clearly demonstrates that both the pH of the reaction and the nature of surfactant define the final morphology of ZnO nanostructures in mechanochemical synthesis.

The observed morphologies for the samples prepared at different reaction conditions can be understood considering the polar nature of ZnO, roles of hydrolyzing agent and surfactant on the modification of surface energy of its different facets or crystal planes.

The commonly accepted growth process of ZnO crystallites in basic aqueous medium can be described through the reactions (Huang *et al.*, 2010; Morales Flores *et al.*, 2014):

$$Zn^{2+} + 2OH^- \rightarrow Zn(OH)_2 \downarrow \quad (2)$$

$$Zn(OH)_2 + 2OH^- \rightarrow Zn(OH)_4^{2-} \quad (3)$$

$$Zn(OH)_4^{2-} \rightarrow ZnO + H_2O + 2OH^- \quad (4)$$

In basic solution, where OH^- ions are abundant, first the Zn^{2+} ions form $Zn(OH)_2$ precipitate following the reaction (2). For highly basic solution, the formed $Zn(OH)_2$ precipitate dissolves almost immediately by reacting with excess OH^- ions, forming $Zn(OH)_4^{2-}$ ions following reaction (3). The $Zn(OH)_4^{2-}$ growth units combine with each other and dehydrate to form ZnO nuclei simultaneously (Equation 4). Through a self-assembly or oriented attachment of the nuclei, elongated ZnO nanostructures are formed with preferred *c*-axis orientation. In the case of solvent-free mechanochemical synthesis, absence of a solvent inhibits the formation of metal ions and hence the formation of $Zn(OH)_2$. The reaction in highly basic condition favors a direct formation of $Zn(OH)_4^{2-}$ and its fast dehydration to form ZnO nuclei. Although the growth habit of ZnO crystal is mainly driven by its intrinsic structure, external parameters such as the presence of surfactant and pH of the reaction have significant effects (Bai *et al.*, 2010). Addition of cationic CTAB in the reaction solution not only reduces its surface tension, reducing the energy of formation of ZnO, induces the formation of CTA^+-$Zn(OH)_4^{2-}$ ion-pair, enhancing the transport of $Zn(OH)_4^{2-}$ units (Yan *et al.*, 2001) and hence the growth rate of ZnO nanostructures. As we see in the Fig. 2 (sample ZnO-2), incorporation of CTAB in the ZnAc-NaOH mixture of 1:3 molar ratio results ZnO nanorods of longer dimension and smaller diameters than the elongated nanoparticles formed in its absence (sample ZnO-1). Incorporation of additional NaOH in the reaction mixture results the formation of longer ZnO nanorods emanating from a common point of nucleation as seen for the sample ZnO-3. In fact, addition of excess NaOH in the reaction mixture enhances the hydrolysis and condensation rates in presence of water molecules (whatever adsorbed by NaOH during mechanochemical processing). Such uncontrolled and unselective hydrolysis/condensation leads to the formation of highly branched or flower-like structures, irrespective of the nature of added surfactant. In the case of PVP, as it is a nonionic surfactant, its addition in reaction mixture reduces surface energy of all the crystal faces of ZnO nuclei due to nonselective adherence, producing nanostructures of spherical morphology as seen for the sample ZnO-4. Again, the incorporation of additional NaOH in the reaction mixture causes a reduction of surface tension, enhancing the growth rate of ZnO. However, in contrast to the earlier case, where CTAB was utilized as surfactant, due to nonionic nature of PVP, no ion-pair is formed. Instead, the excess OH^- ions get attached to the polar surface of positive charge, i.e. the <001> face, probably forming a negatively charged dielectric double-layer, hindering its further growth. As a result, the growth of ZnO along its *c*-axis reduces and the planer or flatter nanostructures of plate-like or sheet-like morphology evolve. Again, an uncontrolled hydrolysis/condensation at high NaOH concentration leads to the formation of flower-like aggregates of thin sheets. In fact, both the evolution of rod-like and plate-like ZnO nanostructures induced by surfactant (Li *et al.*, 2008) and the pH of reaction mixture (Wahab *et al.*, 2009) have been reported in the literature for hydrothermal and precipitation synthesis, respectively.

To study the crystallinity and lattice defects, high resolution TEM images of the typical rod-shaped (ZnO-

2), spherical (ZnO-4) and petal-shaped (ZnO-5) ZnO nanostructures have been recorded (Fig. 3). As can be seen from Figure 3, all the nanostructure are well crystalline with occasional presence of lattice distortion and point defects (indicated by red arrows). Fast Fourier Transform (FFT) of selected areas of the HRTEM images of all three sample (insets of Fig. 3) revealed well defined points patterns correspond to their crystalline nature. It is interesting to note that the rod-shaped nanostructures (sample ZnO-2) contain higher structural defects than the spherical (sample ZnO-4) and petal-shaped (sample ZnO-5) nanostructures. The higher defect content in the ZnO-2 sample is also revealed in its FFT pattern where the diffraction spots are elongated due to structural disorder.

The crystallinity and lattice defects of the nanostructures were studied further recording their room temperature Raman spectra presented in Fig. 4. To understand the effect of surfactant and hydrolyzing agent (NaOH) separately, the results are presented in two groups: Samples prepared using CTAB (Fig. 4a) and the samples prepared with PVP (Fig. 4b). Nanostructures of both the groups revealed well resolved Raman bands corresponding to fundamental and multiphonon modes of crystalline ZnO.

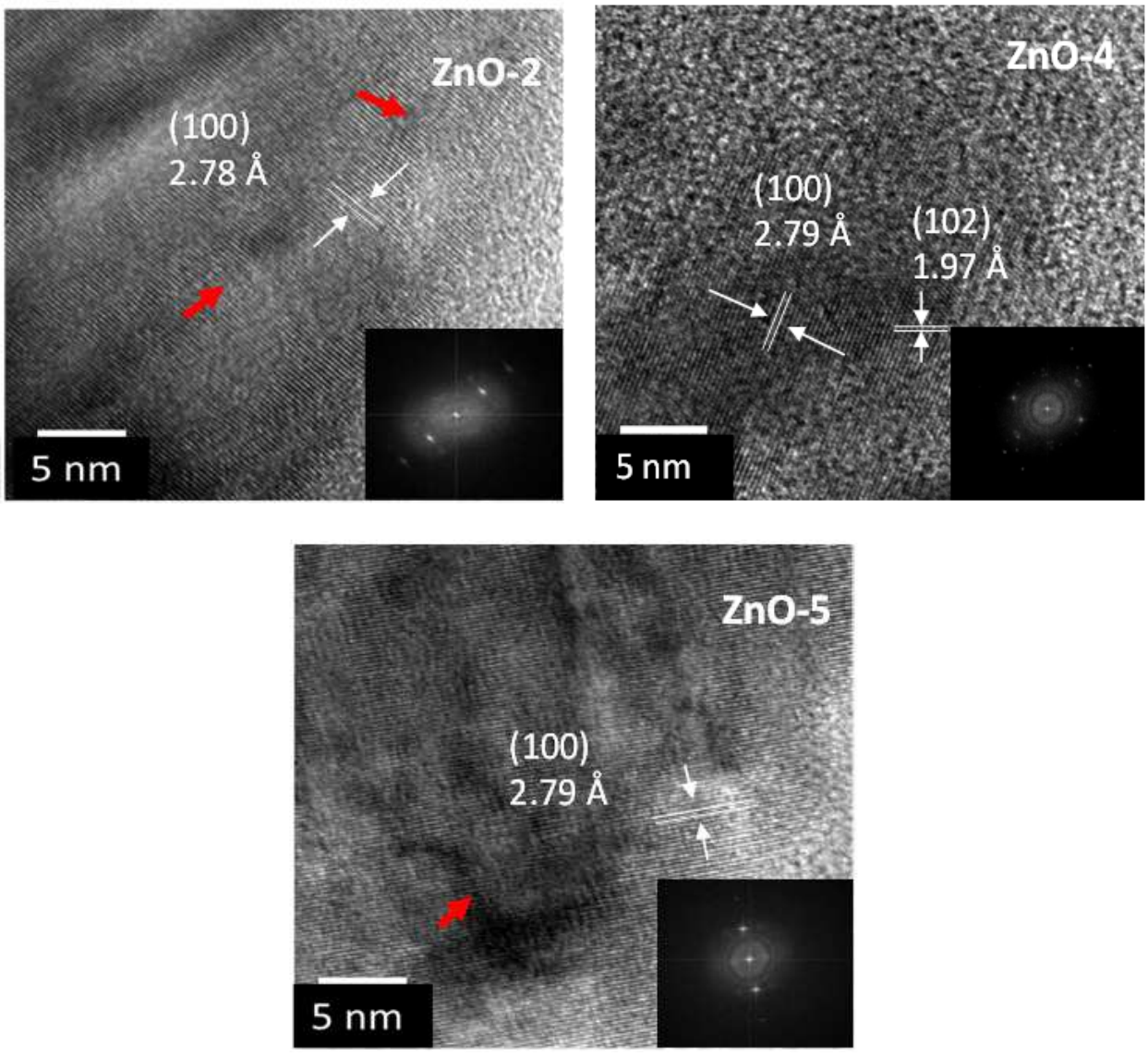

Fig. 3. Typical high resolution TEM micrographs of the rod-shaped (ZnO-2), spherical (ZnO-4) and petal-shaped (ZnO-5) ZnO nanostructures and their corresponding FFTs (insets). Defects like vacancies and lattice distortion are shown by arrows in red color

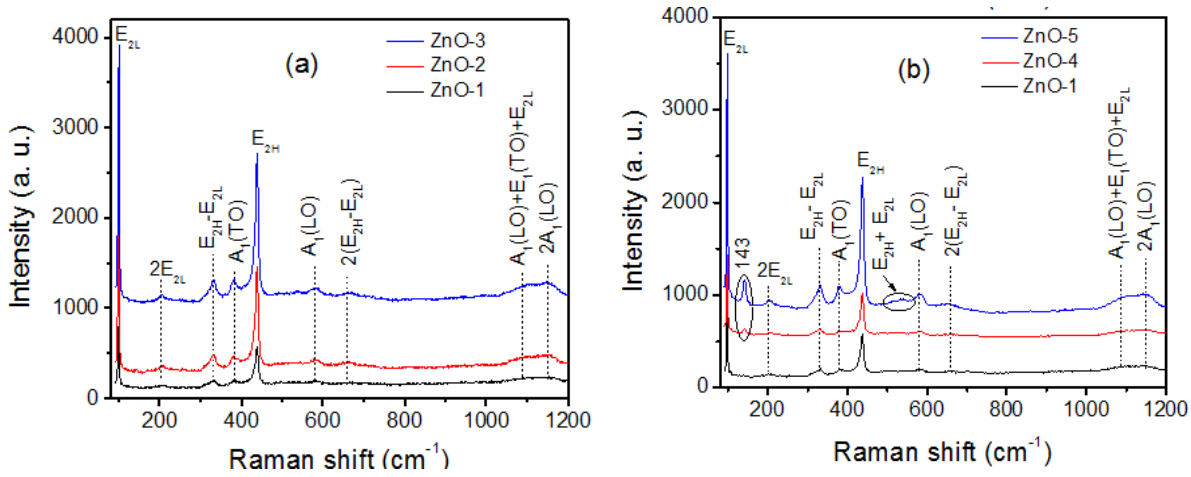

Fig. 4. Room temperature Raman spectra of the ZnO nanostructures synthetized using (a) CTAB and (b) PVP as surfactant

The intense bands revealed around 100 and 439 cm^{-1} correspond to the E_{2L} and E_{2H} modes of nonpolar optical phonons, respectively, characteristic of wurtzite hexagonal ZnO (Morkoç and Özgür, 2008). The Raman bands appeared around 381 and 582 cm^{-1} are the transverse optical (TO) and longitudinal optical (LO) modes of polar A_1 mode. Raman spectra of all the samples revealed two weak bands around 204 and 1150 cm^{-1}, which correspond to second-order processes, attributed to $2E_{2L}$ and $2A_1(LO)$ phonon modes of ZnO, respectively. Moreover, all the Raman bands associated to common multi-phonon processes in ZnO such as E_{2H}-E_{2L} (at 333 cm^{-1}), $2(E_{2H}$-$E_{2L})$ (at 665 cm^{-1}) and $A_1(LO)+E_1(TO)+E_{2L}$ (at 1090 cm^{-1}) were evolved in the ZnO nanostructures, demonstrating clearly their high crystalline quality. For the samples synthetized using PVP as surfactant, there appeared two weaker bands around 538 and 143 cm^{-1}, which did not appear for the samples prepared with CTAB. While the earlier band is associated to $E_{2H}+E_{2L}$ multiphonon in ZnO lattice, the later band has been found at low temperature microRaman spectra of ZnO and assigned to intrinsic defects associated with synthesis process (Cuscó *et al.*, 2007).

As one of the aims of this study is to utilize fabricated ZnO nanostructures as photocatalyst, their surface area and texture have been estimated form nitrogen adsorption-desorption isotherms at 77 K. The adsorption-desorption isotherms of the samples presented in Fig. 5 are typical type III isotherms in Brunauer classification, with no limiting adsorption at high relative pressure. The hysteresis loops can be ascribed to type H3 of mesoporous material according to the IUPAC classification (Lu *et al.*, 2012). Estimated BET specific surface areas of the nanostructures are presented in Table 2. As we see, the estimated specific surface area of the samples vary in between 6.9 to 16.35 $m^2\ g^{-1}$; highest for the sample ZnO-1 (prepared with no surfactant, ZnAc:NaOH = 1:3) and lowest for ZnO-5 (prepared with PVP, ZnAc:NaOH = 1:9). On the other hand, the average pore size in the nanostructures estimated using BET analysis varied in between 30.1 (sample ZnO-2) and 80.5 nm (sample ZnO-4). As it can be noticed, the estimated average pore size of most of the samples is beyond mesoporous limit (2-50 nm). Such high average pore size values estimated for the nanostructures clearly demonstrate that they correspond to inter-particle spaces, rather than the porosity of individual nanostructure. In fact, the pore size distribution of all the samples through Barrett-Joyner-Halenda (BJH) (Barrett *et al.*, 1951) analysis revealed a prominent peak at around 1.64 nm pore radius, along with some broader distributions at higher values (insets of Fig. 4).

As it is well known, on illumination with high energy light, the valance band electrons of ZnO get promoted to its conduction band, creating electron-hole pairs (Equation 5), which diffuse to the surface of the semiconductor:

$$ZnO + h\nu \rightarrow ZnO + h^{+}_{VB} + e^{-}_{CB} \quad (5)$$

The photo-generated holes near the nanostructure surface react with surface OH^- groups and H_2O molecules to produce $HO^{\bullet}$ radicals (Equation 6 and 7), which get adsorbed at the catalyst surface. The surface adsorbed $HO^{\bullet}$ radicals are strong oxidizing agents, which react with surface adsorbed organic dye molecules such as MB, mineralizing them partially or completely following the reaction (Equation 8):

$$h^{+}_{VB} + H_2O \rightarrow OH^{-} + H^{+} \quad (6)$$

$$h^{+}_{VB} + OH^{-} \rightarrow HO^{\bullet} \quad (7)$$

$$HO^{\bullet} + MB \rightarrow \text{degradation of } MB \quad (8)$$

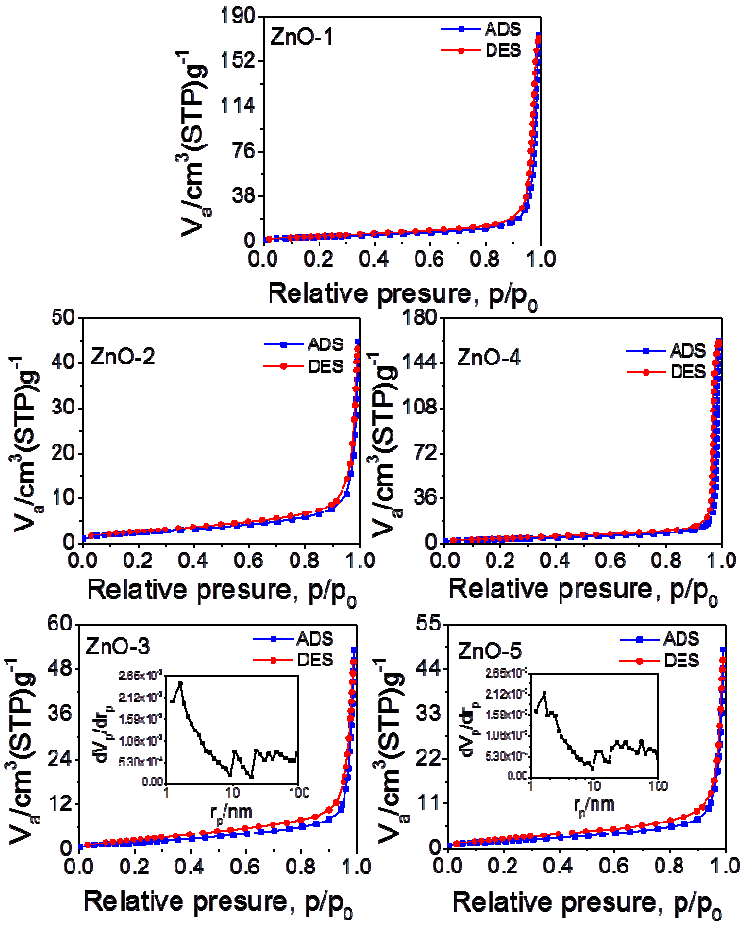

Fig. 5. N_2 adsorption-desorption isotherms of the ZnO nanostructures measured at 77K. The insets are the pore size distributions (BJH-plots) of corresponding samples

Table 2. Pseudo-first-order rate constant (k), the half-life ($t_{1/2}$) and R^2 of MB degradation by the ZnO nanostructures fabricated by mechanochemical synthesis with comparison with their specific surface area and surface basics sites

Sample	BET surface area (m^2/g)	Density of basic sites (g^{-1} catalyst)	k (min^{-1})	$t_{1/2}$ (min)	R^2
ZnO-1	16.35	8.95×10^{13}	2.71×10^{-2}	27.5	0.999
ZnO-2	8.72	1.03×10^{14}	4.71×10^{-2}	17.5	0.998
ZnO-3	8.35	7.99×10^{13}	3.87×10^{-2}	22.5	0.997
ZnO-4	12.36	7.87×10^{13}	3.24×10^{-2}	24.0	0.995
ZnO-5	6.90	1.06×10^{14}	2.03×10^{-2}	40	0.986

On the other hand, the electrons in the conduction band can reduce O_2 to produce superoxide radicals $O_2^{\bullet}$ (Equation 9), which subsequently react with hydrogen ions generated through water splitting to form hydroperoxyl $HO_2^{\bullet}$ (Equation 10) radical and other reactive oxygen species such as H_2O_2 and $OH^{\bullet}$ (Equation 11 and 12):

$$O_2 + e_{CB}^- \rightarrow O_2^{\bullet} \quad (9)$$

$$O_2^{\bullet} + H^+ \rightarrow HO_2^{\bullet} \quad (10)$$

$$2OH^{\bullet} \rightarrow H_2O_2 \quad (11)$$

$$H_2O_2 + e_{CB}^- \rightarrow HO^{\bullet} + OH^- \quad (12)$$

Photocatalytic degradation of most of the organic compounds in a heterogeneous system follows first-order kinetics (Serrano *et al.*, 2004; Yadav *et al.*, 2007), for which the steady-state photocatalytic rate can be expressed through Langmuir–Hinshelwood relation. The photocatalytic degradation of MB by the ZnO nanostructures grown at different reaction conditions

obeyed the pseudo-first-order kinetics. The photo degradation rate of MB for low initial concentration can be expressed as:

$$\ln C = \ln C_0 - kt \quad (13)$$

Or:

$$\ln(C / C_0) = -kt \quad (14)$$

where, k is the pseudo-first-order rate constant, C_0 is the initial concentration of MB in reaction solution and C is the MB concentration in reaction solution after time t of UV illumination.

The reduction of MB content in catalytic solution upon UV irradiation for a typical sample (ZnO-2), the plots of C/C_0 versus irradiation time and $\ln(C/C_0)$ versus irradiation time for all the nanostructures are shown in Fig. 6. The linear relationship between $\ln(C/C_0)$ and the UV illumination time (Fig. 6C) clearly demonstrates the photo-degradation process follows first-order kinetics. The values of the pseudo-first-order rate constant k estimated from the linear regression curves (linear fits), the estimated values of $t_{1/2}$ (dye half-life) and corresponding correlation coefficients (R^2) for the ZnO nanostructures are presented in Table 2. We can see that the sample ZnO-2 prepared using CTAB at ZnAc:NaOH = 1:3 molar ratio has highest rate constant ($k = 4.71\times10^{-2}$ min^{-1}) and lowest $t_{1/2}$ (17.5 min) among the nanostructures, indicating their excellent photocatalytic activity for MB degradation. From the data presented in Table 1 and 2, we can see that all the nanostructures have near-stoichiometric composition with minor variation of average crystallite size (32-38 nm). However, due to morphological diversity, the BET surface area and BET pore size in the nanostructures varied. As apart from surface area, pore size and crystallite size, the photocatalytic activity of metal-oxide nanostructures depend on the density of basic (OH^-) or acid sites at their surfaces, a quick and fast quantitative measurement of basic sites was performed following the method described by Corro *et al.* (2014). As the nanostructures were fabricated in highly basic conditions, the density of basic sites at their surface was very high (Table 2), which is responsible for their enhanced dye adsorption capacity.

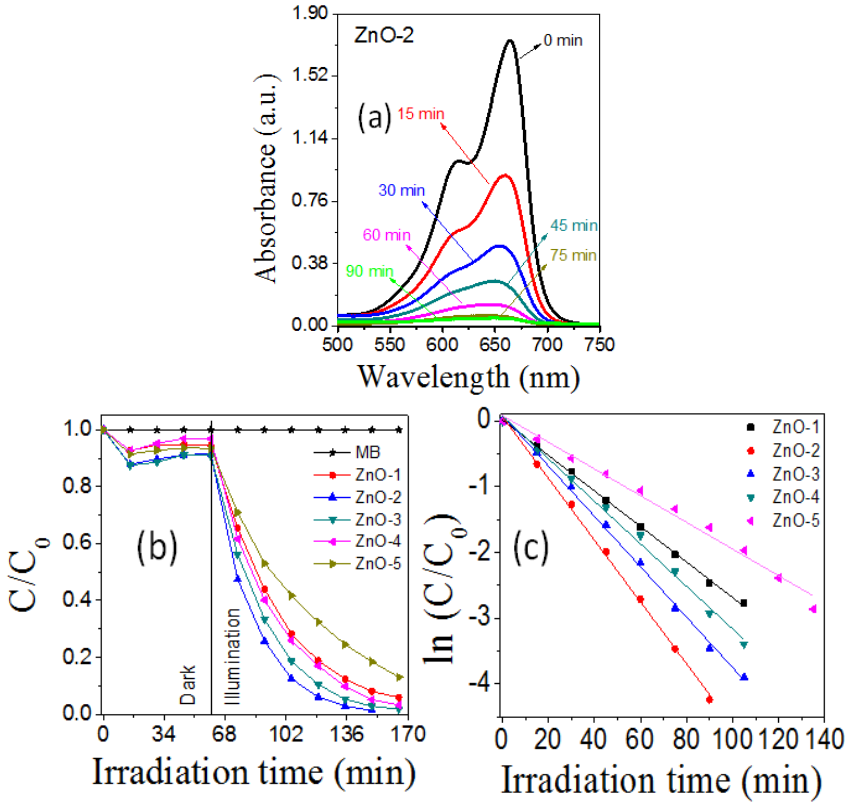

Fig. 6. (a) MB absorption spectra used to monitor the photocatalytic degradation rate for the sample ZnO-2, (b) photo-degradation rate of MB over the ZnO nanostructures prepared at different conditions and (c) ln (C/C0) Vs irradiation time plots used to evaluate the degradation rate-constants. The MB degradation behavior under UV illumination has also been included in (b) to show that there is no photo-degradation of MB in absence of catalyst

While all the nanostructures fabricated in our soft mechanochemical process present high efficiency for MB degradation under UV illumination, the sample ZnO-2 prepared at ZnAc:NaOH = 1:3 in presence of CTAB revealed best MB degradation performance. The nanostructures of sample ZnO-2 contain highest surface basic sites, bigger average crystallite size, smaller average pore diameter and moderate BET surface area (Table 1 and 2). Therefore, it is very difficult to associate their higher photocatalytic performance to any one of these texture parameters specifically, as have been practiced in a vast number of published works. Considering the morphology and growth habit of all the nanostructures fabricated in this study, it seems, the high photocatalytic performance of the well dispersed rod-like nanostructures of ZnO-2 sample is due to the high exposure of their non-polar facets, which do not adsorb MB molecules as strongly as polar surfaces.

A strong adsorption of cationic dye over polar surface of ZnO probably blocks the penetration of exciting UV radiation, responsible for generating electron-hole pairs at semiconductor surface. On the other hand, the electron mobility in flater ZnO surface such as nanopetals is expected to be higher than other surfaces due to their directional and uninterrupted conduction channel. The high electron mobility of semiconductor surface would increase the recombination rate of photo-generated electrons and holes, which is unfavorable for photcatalytic process.

Conclusion

In summary, ZnO nanostructures of different morphologies could be fabricated in large scale and controlled manner through solvent-free mechanochemical process by controlling the precursor to hydrolyzer molar ratio and suitable choice of surfactant. Apart from its cheapness, the process can produce near-stoichiometric ZnO nanostructures with enhanced photocatalytic performance for cationic dye degradation under UV illumination. The high concentration of basic sites at the surface of the nanostructures is the principal responsible for their high photocatalytic activity. However, due to polar nature of ZnO crystals, the orientation of crystal facets exposed to the reaction mixture also plays a significant role on their photocatalytic performance. The ZnO nanostructures fabricated by our soft mechanochemical synthesis process can mineralize 50% of MB molecules in aqueous solution as fast as in 17.5 min. The large scale production ability, low cost processing and high dye degradation ability of the fabricated nanostructures suggest the solvent-free mechanochemical process is extremely attractive for fabricating ZnO nanostructures for dye removal from industrial effluents.

Acknowledgement

The work was financially supported by VIEP-BUAP and CUVyTT-BUAP and CONACYT, Mexico, through the grants # VIEP/EXC/2015-205, DITCo-2015-38 and INFR-2011-1-163153, respectively.

Author's Contributions

Raúl Sánchez Zeferino: Synthesized the ZnO nanostructures.

Jesús Alberto Ramos Ramón: Performed surface area and texture characterization of the nanostructures.

Eunice De Anda Reyes: Performed the photocatalytic characterization of the nanostructures.

Rutilo Silva González: Performed morphology and composition evaluation of the nanostructures.

Umapada Pal: Planned and coordinated the research, analyzed the results and wrote the article.

Ethics

This article is original and contains unpublished material. The corresponding author confirms that all of the other authors have read and approved the manuscript and no ethical issues involved.

References

An, S., S. Partk, H. Ko, C. Jin and W.I. Lee *et al*., 2013. Enhanced gas sensing properties of branched ZnO nanowires. Thin Solid Films, 547: 241-245. DOI: 10.1016/j.tsf.2013.02.021

Anand, K., S. Varghese and T. Kurian, 2014. Synthesis of ZnO nanorods through mechano-chemical route: A solvent free approach. Int. J. Theo. Applied Sci., 6: 87-93.

Bai, S., L. Chen, D. Li, W. Yang and P. Yang *et al*., 2010. Different morphologies of ZnO nanorods and their sensing property. Sens. Actuators B, 146: 129-137. DOI: 10.1016/j.snb.2010.02.011

Barrett, E.P., L.G. Joyner and P.P. Halenda, 1951. The determination of pore volume and area distributions in porous substances. I. Computations from nitrogen isotherms. J. Am. Chem. Soc., 73: 373-380. DOI: 10.1021/ja01145a126

Brunauer, S., P.H. Emmett and E. Teller, 1938. Adsorption of gases in multimolecular layers. J. Am. Chem. Soc., 60: 309-319. DOI: 10.1021/ja01269a023

Chen, D., X. Jiao and G. Cheng, 2000. Hydrothermal synthesis of zinc oxide powders with different morphologies. Solid State Commun., 113: 363-366. DOI: 10.1016/S0038-1098(99)00472-X

Chen, X., F. Zhang, Q. Wang, X. Han and X. Li *et al*., 2015. The synthesis of ZnO/SnO_2 porous nanofibers for dye adsorption and degradation. Dalton Trans., 44: 3034-3042. DOI: 10.1039/C4DT03382E

Corro, G., F. Bañuelos, E. Vidal and S. Cebada, 2014. Measurements of surface acidity of solid catalysts for free fatty acids esterification in jatropha curcas crude oil for biodiesel production. Fuel, 115: 625-628. DOI: 10.1016/j.fuel.2013.07.060

Cullity, B.D. and S.R. Stock, 1956. Elements of X-Ray Diffraction. 1st Edn., Addison-Wesley Publishing Company, Inc., Massachusetts, ISBN-10: 0201610914, pp: 514.

Cuscó, R., E. Alarcón-Lladó, J. Ibáñez, L. Artus and J. Jimenez *et al*., 2007. Temperature dependence of Raman scattering in ZnO. Phys. Rev. B, 75: 165202-11. DOI: 10.1103/PhysRevB.75.165202

Hahn, Y.B., R. Ahmad and N. Tripathy, 2012. Chemical and biological sensors based on metal oxide nanostructures. Chem. Commun., 48: 10369-10385. DOI: 10.1039/C2CC34706G

He, J.H., J.H. Hsu, C.W. Wang, H.N. Lin and L.J. Chen *et al*., 2006. Pattern and feature designed growth of ZnO nanowire arrays for vertical devices. J. Phys. Chem. B, 110: 50-53. DOI: 10.1021/jp055180j

Hilger, I. and W.A. Kaiser, 2012. Iron oxide-based nanostructures for MRI and magnetic hyperthermia. Nanomedicine, 7: 1443-1459. DOI: 10.2217/NNM.12.112

Huang, J.R., Y.J. Wu, C.P. Gu, M.H. Zhai and K. Yu *et al*., 2010. Large-scale synthesis of flowerlike ZnO nanostructure by a simple chemical solution route and its gas-sensing property. Sens. Actuators B, 146: 206-212. DOI: 10.1016/j.snb.2010.02.052

Hsu, Y.F., Y.Y. Xi, K.H. Tam, A.B. Djurišić and J. Luo *et al*., 2008. Undoped p-type ZnO nanorods synthesized by a hydrothermal method. Adv. Funct. Mater., 18: 1020-1030. DOI: 10.1002/adfm.200701083

Jalali, N., J. Briscoe, P. Woolliams, M. Stewart and P.M. Weaver *et al*., 2013. Passivation of zinc oxide nanowires for improved piezoelectric energy harvesting devices. J. Phys., 476: 012131-1-012131-6. DOI: 10.1088/1742-6596/476/1/012131

Jang, J.M., S.D. Kim, H.M. Choi, J.Y. Kim and W.G. Jung, 2009. Morphology change of self-assembled ZnO 3D nanostructures with different pH in the simple hydrothermal process, Mater. Chem. Phys., 113: 389-394. DOI: 10.1016/j.matchemphys.2008.07.108

Jia, X., M. Tian, Y. Liu, X. Wu and H. Song, 2015. In situ precipitation preparation of ZnO hollow spheres and their photocatalysis and gas sensing properties. Appl. Phys. A, 119: 1179-1185. DOI: 10.1007/s00339-015-9088-1

Khosla, E., S. Kaur and P.N. Dave, 2015. Ionic dye adsorption by zinc oxide nanoparticles. Chem. Ecol., 31: 173-185. DOI: 10.1080/02757540.2014.907281

Kumar, R., O. Al-Dossary, G. Kumar and A. Umar, 2015. Zinc oxide nanostructures for NO_2 Gas-Sensor applications: A review. Nano-Micro Lett., 7: 97-120. DOI: 10.1007/s40820-014-0023-3

Lorenz, H., M. Friedrich, M. Armbrüster, B. Klötzer and S. Penner, 2013. ZnO is a CO_2 selective steam reforming catalyst. J. Catal., 297: 151-154. DOI: 10.1016/j.jcat.2012.10.003

Li, F., L. Hu, Z. Li and X. Huang, 2008. Influence of temperature on the morphology and luminescence of ZnO micro and nanostructures prepared by CTAB-assisted hydrothermal method. J. Alloy Comp., 465: L14-L19. DOI: 10.1016/j.jallcom.2007.11.009

Lu, A.H., D. Zhao and Y. Wan, 2012. Nanocasting: A Versatile Strategy for Creting Nanostructured Porous Materials. 1st Edn., RSC Publishing, ISBN-13: 978-0-85404-188-6.

Matsamura, Y. and H. Ishibe, 2009. Suppression of CO by-production in steam reforming of methanol by addition of zinc oxide to silica-supported catalyst. J. Catal., 268: 282-289. DOI: 10.1016/j.jcat.2009.09.026

Morales Flores, N., U. Pal, R. Galeazzi and A. Sandoval, 2014. Effects of morphology, surface area and defect contento n the photocatalytic dye degradation performance of ZnO nanostructures. RSC Adv., 4: 41099-41110. DOI: 10.1039/c4ra04552j

Morkoç, H. and Ü. Özgür, 2008. Zinc Oxide: Fundamentals, Materials and Device Technology. 1st Ed., John Wiley and Sons, Germany, ISBN-10: 3527623957, pp: 500.

Ni, Y.H., X.W. Wei, X. Ma and J.M Hong, 2005. CTAB assited one-pot hydrothermal synthesis of columnar hexagonal-shaped ZnO cystals. J. Cryst. Growth, 283: 48-56. DOI: 10.1016/j.jcrysgro.2005.05.048

Norman, V.J., 1970. The adsorption of dyes on zinc oxide: The effect of non-stoicheiometry. Aust. J. Chem., 23: 2171-2176. DOI: 10.1071/CH9702171

Olson, D.C., Y.J. Lee, M.S. White, N. Kopidakis and S.E. Shaheen *et al*., 2007. Effect of polymer processing on the performance of poly(3-hexylthiophene)/ZnO nanorod photovoltaic devices. J. Phys. Chem. C, 111: 16640-16645. DOI: 10.1021/jp0757816

Pan, T.C., Y.C. Chen, C.C. Hsieh, C.H. Lin and C.Y. Su *et al*., 2014. Ultrasonic sensing device with ZnO piezoelectric nanorods by selectively electrospraying method. Sensors Actuators A, 216: 318-327. DOI: 10.1016/j.sna.2014.05.024

Ruiz Peralta, M.L., U. Pal and R. Sánchez Zeferino, 2012. Photoluminescence (PL) quenching and enhanced photocatalytic activity of Au-decorated ZnO nanorods fabricated through microwave-assisted chemical synthesis. ACS App. Mater. Interfaces, 4: 4807-4816. DOI: 10.1021/am301155u

Serrano, J., A.H. Romero, F.J. Manjon, R. Lauck and M. Cardona *et al*., 2004. Pressure dependence of the lattice dynamics of ZnO: An *ab initio* approach. Phys. Rev. B: Condens. Matter Mater. Phys., 69: 094306. DOI: 10.1103/PhysRevB.69.094306

Shao, S., P. Jia, S. Liu and W. Bai, 2008. Stable field emission from rose-like zinc oxide nanostructures synthesized through a hydrothermal route. Mater. Lett., 62: 1200-1203. DOI: 10.1016/j.matlet.2007.08.049

Shen, L., L. Guo, N. Bao and K. Yanagisawa, 2003. Salt-assited solid-state chemical reaction. Synthesis of ZnO nanocrystals. Chem. Lett., 32: 826-827. DOI: 10.1246/cl.2003.826

Solanki, P.R., A. Kaushik, V.V. Agrawal and B.D. Malhotra, 2011. Nanostructured metal oxide-based biosensors. NPG Asia Mater., 3: 17-24. DOI: 10.1038/asiamat.2010.137

Spencer, M.S., 1999. The role of zinc oxide in Cu/ZnO catalysts for methanol synthesis and water-gas shift reaction. Top. Catal., 8: 259-266. DOI: 10.1023/A:1019181715731

Tak, Y. and K. Yong, 2005. Controlled growth of well-aligned ZnO nanorod array using a novel solution method. J. Phys. Chem. B, 109: 19263-19269. DOI: 10.1021/jp0538767

Tsuzuki, T. and P.G. McCormick, 2001. ZnO nanoparticles synthesized by mechanochemical processing. Scripta Mater., 44: 1731-1734. DOI: 10.1016/S1359-6462(01)00793-X

Tsuzuki, T. and P.G. McCormick, 2004. Mechanochemical synthesis of nanoparticles. J. Mater. Sci., 39: 5143-5146. DOI: 10.1023/B:JMSC.0000039199.56155.f9

Valerini, D., A.P. Caricato, M. Lomascolo, F. Romano and A. Taurino *et al*., 2008. Zinc oxide nanostructures grown by pulsed laser deposition. Appl. Phys. A, 93: 729-733. DOI: 10.1007/s00339-008-4703-z

Wahab, R., Y.S. Kim and H.S. Shin, 2009. Synthesis, characterization and effect of pH variation on zinc oxide nanostructures. Mater. Trans., 50: 2092-2097. DOI: 10.2320/matertrans.M2009099

Wang, J.X., X.W. Sun, Y. Yang, H. Huang and Y.C. Lee *et al*., 2006. Hydrothermally grown oriented ZnO nanorod arrays for gas sensing applications. Nanotechnology, 17: 4995-4998. DOI: 10.1088/0957-4484/17/19/037

Wang, L., Y. Kang, X. Liu, S. Zhang and W. Huang *et al*., 2012. ZnO nanorod gas sensor for ethanol detection. Sensors Actuators B, 162: 237-243. DOI: 10.1016/j.snb.2011.12.073

Wang, L., X. Zhang, S. Zhao, G. Zhou and Y. Zhou *et al*., 2005. Synthesis of well-aligned ZnO nanowires by simple physical deposition on c-oriented ZnO thin films without catalysts or additives. Appl. Phys. Lett., 86: 024108-1-024108-3. DOI: 10.1063/1.1851607

Wang, X., C.J. Summers and Z.L. Wang, 2004. Large-scale hexagonal-patterned growth of aligned zno nanorods for nano-optoelectronics and nanosensor arrays. Nano Lett., 4: 423-426. DOI: 10.1021/nl035102c

Wang, X., Y. Ding, C.J. Summers and Z.L. Wang, 2004. Large-scale synthesis of six-nanometer-wide ZnO nanobelts. J. Phys. Chem. B, 108: 8773-8777. DOI: 10.1021/jp048482e

Wang, Z.L. and J. Song, 2006. Piezoelectric nanogenerators based on zinc oxide nanowire arrays. Science, 312: 242-246. DOI: 10.1126/science.1124005

Xie, J., P. Li, Y.J. Wang and Y. Wei, 2009. Synthesis of needle- and flower-like ZnO microstructures by a simple aqueous solution route. J. Phys. Chem. Solids, 70: 112-116. DOI: 10.1016/j.jpcs.2008.09.014

Xie, J., Y. Li, W. Zhao, L. Bian and Y. Wei, 2011. Simple fabrication and photocatalytic activity of ZnO particles with different morphologies. Powder Technol., 207: 140-144. DOI: 10.1016/j.powtec.2010.10.019

Xu, J., Q. Pan, Y. Shun and Z. Tian, 2000. Grain size control and gas sensing properties of ZnO gas sensor. Sensors Actuators B, 66: 277-279. DOI: 10.1016/S0925-4005(00)00381-6

Yadav, H.K., K. Sreenivas, R.S. Katiyar and V. Gupta, 2007. Defect induced activation of Raman silent modes in rf co-sputtered Mn doped ZnO thin films. J. Phys. D, 40: 6005-6009. DOI: 10.1088/0022-3727/40/19/034

Yan, L., Y. Li, Z.X. Deng, J. Zhuang and X. Sun, 2001. Surfactant-assisted hydrothermal synthesis of hydroxyapatite nanorods. Int. J. Inorg. Mater., 3: 633-637. DOI: 10.1016/S1466-6049(01)00164-7

Yang, L., X. Kong, J. Wang, M. Pan and W. Yang *et al*., 2015. Synthesis and photocatalytic performance of ZnO hollow spheres and porous nanosheets. J. Mater. Sci. DOI: 10.1007/s10854-015-3738-0

Zhang, Z., M. Lu, H. Xu and W.S. Chin, 2007. Shape-controlled synthesis of zinc oxide: A simple method for the preparation of metal oxide nanocrystals in non-aqueous medium. Chem. Euro. J., 13: 632-638. DOI: 10.1002/chem.200600293

Zimmler, M.A., D. Stichtenoth, C. Ronning, W. Yi and V. Narayanamurti *et al*., 2008. Scalable fabrication of nanowire photonic and electronic circuits using spin-on glass. Nano Lett., 8: 1695-1699. DOI: 10.1021/nl080627w